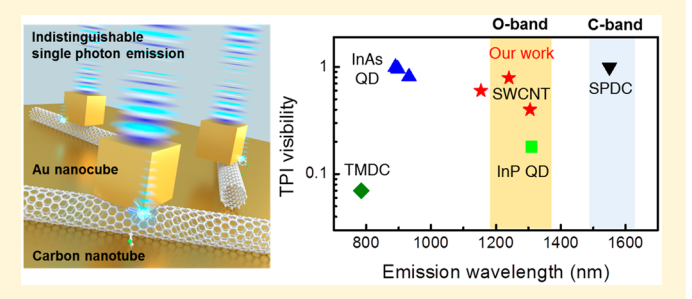


# Carbon Nanotube Color Centers in Plasmonic Nanocavities: A Path to Photon Indistinguishability at Telecom Bands

Yue Luo,<sup>†,‡,§</sup> Xiaowei He,<sup>†,‡</sup> Younghee Kim, Jeffrey L. Blackburn, Stephen K. Doorn, Han Htoon,\*\* and Stefan Strauf\*\*, Too

Supporting Information

ABSTRACT: Indistinguishable single photon generation at telecom wavelengths from solid-state quantum emitters remains a significant challenge to scalable quantum information processing. Here we demonstrate efficient generation of "indistinguishable" single photons directly in the telecom O-band from aryl-functionalized carbon nanotubes by overcoming the emitter quantum decoherence with plasmonic nanocavities. With an unprecedented single-photon spontaneous emission time down to 10 ps (from initially 0.7 ns) generated in the coupling scheme, we show a two-photon



interference visibility at 4 K reaching up to 0.79, even without applying post selection. Cavity-enhanced quantum yields up to 74% and Purcell factors up to 415 are achieved with single-photon purities up to 99%. Our results establish the capability to fabricate fiber-based photonic devices for quantum information technology with coherent properties that can enable quantum

KEYWORDS: Plasmonic nanocavities, carbon nanotubes, indistinguishable single photons, telecommunication bands

igcup olid-state single photon emitters (SPEs) are a fundamental resource to realize scalable applications for quantum information processing and quantum key distribution (QKD).<sup>1-3</sup> Whereas most SPE materials generate a stream of incoherent single photons, coherent quantum emission in the form of "indistinguishable" single photons is required for advanced quantum state operations to enable quantum memory<sup>4,5</sup> and quantum repeater protocols.<sup>6</sup> The fundamental challenge to realize coherent SPEs is the underlying quantum decoherence that results from exciton-bath interactions, leading to coherence times  $(T_2)$  that are typically much shorter than the spontaneous emission (SE) lifetime  $(T_1)$ , that is, emission far from the ideal Fourier transform limit of  $T_2$ /  $2T_1 = 1$ . Possible solutions to overcome this limitation involve cryogenic cooling to reduce phonon dephasing combined with coupling to dielectric cavities to enhance the  $T_1$  time via the Purcell effect. In this way, a high degree of indistinguishability was achieved for the single photon emission from semiconductor quantum dots (QDs) in the 900 nm band, which benefit already from moderate Purcell factors provided by dielectric cavities, because they have intrinsically long  $T_2$ 

The demonstrated coherent quantum light emission in the 900 nm band is however rather limited with respect to applications in quantum information science. Ideally, the underlying quantum materials emit directly into a desired telecom band to enable high-throughput fiber-based quantum networks without the need for a priori lossy frequency conversion through nonlinear optical processes. 10 Unfortunately, most SPEs, such as QDs, 7-9 color centers in diamond, 11 silicon carbide, 12 or hexagonal boron nitride, 13 emit outside of the relevant telecom bands (1.3-1.55  $\mu$ m). Although randomly distributed defect centers in GaN14 and SiC<sup>15</sup> have been shown to match the O-band, they lack control of the emission wavelength and photon indistinguishability was not achieved, that is, the single photon emission remains incoherent in these materials due to strong exciton dephasing. So far, only epitaxially grown InAs QDs are able to emit directly in the O-band (1320 nm) and have been shown to display photon indistinguishability at 4 K, albeit at a rather low two-photon interference (TPI) visibility of only 0.18 without

Received: October 2, 2019 Revised: November 1, 2019 Published: November 4, 2019



Department of Physics and <sup>‡</sup>Center for Quantum Science and Engineering, Stevens Institute of Technology, Hoboken, New Jersey 07030, United States

<sup>§</sup>Center for Nanoscale Systems, Harvard University, Cambridge, Massachusetts 02138, United States

Center for Integrated Nanotechnologies, Materials Physics and Applications Division, Los Alamos National Laboratory, Los Alamos, New Mexico 87545, United States

<sup>&</sup>lt;sup>1</sup>National Renewable Energy Laboratory, Golden, Colorado 80401, United States

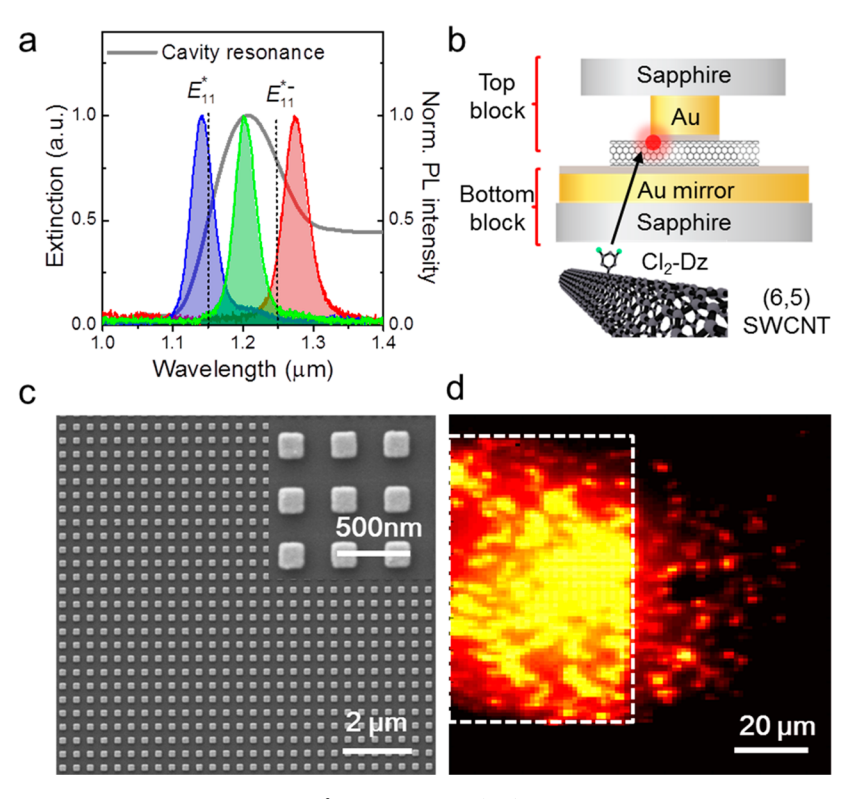


Figure 1. Overview of sample design enabling coupling of sp<sup>3</sup> functionalized (6,5) single-walled carbon nanotubes to plasmonic gap modes. (a) Cavity resonance spectrum (gray solid line) that covers the defect state emission wavelength for both  $E_{11}^*$  and  $E_{11}^{**-}$  excitons of (6,5) SWCNTs. Blue, green, and red are experimental spectra from individual SWCNTs recorded at 300 K. (b) Schematic of sp<sup>3</sup> functionalized SWCNT coupled to plasmonic Au nanocube cavity array. The Au cube and the planar Au mirror are separated by 2 nm  $Al_2O_3$  acting as a dielectric spacer. Carbon nanotube is shown enlarged to highlight the 3,5-dichlorobenzene-diazonium ( $Cl_2$ -Dz) defect site. (c) Scanning electron microscope images of plasmonic nanocube arrays. (Inset: zoomed in to illustrate sharp edges.). (d) Wide-field photoluminescence image collected with 1060 nm long-pass filter. White dash lines indicate the borders of plasmonic nanocube arrays. Contrast is adjusted to show the off-chip SWCNTs.

post selection, partly due to the limited 4-fold Purcell effect of the utilized dielectric cavity<sup>16</sup> (Supporting Information, Supplementary Note 1).

As recently proposed by Bogdanov et al., 17 plasmonic gapmode nanocavities might offer a new path to overcome quantum decoherence, particularly for SPE materials emitting at telecom wavelengths that suffer from strong dephasing, since the subdiffraction limited cavity mode volume is several orders of magnitude smaller compared to dielectric cavities. As a result, the gap-mode that forms between nanoparticle and metal surface at ultrasmall length scales of 2-5 nm is able to drastically minimize ohmic losses that are typical for plasmonic materials at larger length scales, giving rise to significantly faster outcoupling into the far-field compared to the exciton decay time. In this way, the strong enhancement of the lightmatter interaction in plasmonic gap-mode nanocavities can drastically shorten  $T_1$  to potentially approach  $T_2$  even for SPE materials that suffer from fast dephasing, while achieving high quantum yield. Strong light enhancement quantified by Purcell factors  $(F_p)$  up to 1000 have been demonstrated for embedded quantum emitters, fulfilling system-level demands in terms of broadband operation, high internal quantum yield and nearunity extraction efficiency. 18,19 However, experimental demonstration that plasmonic nanocavities can also overcome SPE decoherence to generate indistinguishable single photons remains elusive.

To this end, single-walled carbon nanotubes (SWCNTs) are of great interest because they are solution-based emitters that allow unmatched ability for integration with plasmonic

nanocavities<sup>20</sup> at the required length scales of a few nanometers and have been shown to deliver high purity single-photon states directly in the telecom O-band<sup>21</sup> and Cband<sup>22</sup> under room-temperature conditions. Moreover, the technique of covalent sidewall functionalization via aryl-based sp<sup>3</sup> defect sites<sup>23</sup> not only introduces energetically deep exciton trapping potentials but also enables controlled wavelength tunability due to their structural diversity.<sup>24</sup> Specifically, this approach capitalizes on the sensitivity of covalently generated point defects with precise atomic properties dependent on substituents on the functional group and binding configuration on the nanotube, thereby enabling ultimate control over the quantum properties of the defect site. 22-24 Furthermore, SWCNTs also allow for electroluminescence enabling fully integrated quantum photonic circuits including sender and receiver modules.2

The major challenge for SWCNTs stems from the relatively short  $T_2$  of  $E_{11}$  excitons, ranging from 0.5 to 40 ps,  $^{26-28}$  compared to the several orders of magnitude longer  $T_1$  of typically a few nanoseconds in ultraclean SWCNTs.  $^{27,29}$  It was recently shown that the SE time for the  $E_{11}$  exciton in (6,4) SWCNTs can approach the Fourier transform limit at extreme low pump power when coupled to a plasmonic bowtie antenna. Unfortunately the  $E_{11}$  exciton emission is strongly susceptible to pump-induced dephasing, making detection of single photon indistinguishability for  $E_{11}$  excitons rather difficult. In contrast, the deeply localized exciton states that arise from aryl-functionalized SWCNTs ( $E_{11}^*$  and  $E_{11}^{*-}$ ) are found to be significantly better protected from pump-induced

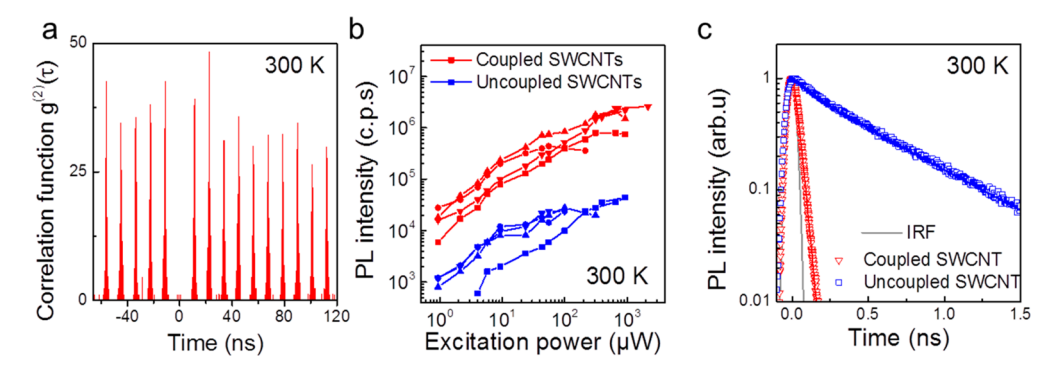


Figure 2. Room-temperature characterization of sp<sup>3</sup> defect-state emission from aryl-functionalized (6,5) SWCNTs coupled to plasmonic nanocavites. (a) Second-order photon correlation function  $g^{(2)}(\tau)$  recorded with a Hanbury-Brown Twiss interferometer under pulsed excitation. The purity of the single photons is characterized by  $g^{(2)}(0) = 0.01 \pm 0.005$ . (b) Excitation power dependence of the integrated exciton emission for the coupled (red symbols) and the uncoupled (blue symbols) case under CW excitation, respectively. (c) Time-resolved photoluminescence intensity for SWCNTs in their uncoupled state (blue squares) and coupled state (red triangles). Blue and red solid lines are deconvolution fits which yield monoexponential decay time of  $\tau_{\text{off,RT}} = 588 \pm 10$  ps and  $\tau_{\text{on,RT}} = 11 \pm 3$  ps. IRF: Instrument response function.

dephasing with 3–6-fold longer  $T_2$  times up to 12 ps,  $^{26,30}$  as well as intrinsic  $T_1$  times up to 1.5 ns.  $^{30,31}$  Previous efforts to couple functionalized SWCNTs emitting at telecom bands to photonic crystal cavities show however only moderate Purcell factors of less than 2-fold,  $^{32}$  whereas generation of indistinguishable photons for carbon nanotubes has not been achieved.

Here we demonstrate that it is possible to overcome the quantum decoherence in the single photon emission from arylfunctionalized (6,5) SWCNTs by coupling to a plasmonic gapmode nanocavity. With cavity-enhanced quantum yields up to 74% and Purcell factors up to 415, we achieve unprecedented single-photon SE times down to 10 ps (from initially 0.7 ns). As a result, our scheme enables transforming the initially incoherent single photon stream of the quantum emitter into a coherent output that is characterized with a TPI visibility up to 0.79 at 4 K, that is, a 99-fold improvement compared to the TPI visibility in the uncoupled case. The generation of highly pure (99%) and indistinguishable single photons with an efficiency of 0.16 photons per pulse is achieved directly in the telecom O-band without relying on quantum frequency conversion, thereby enabling a path toward quantum logic applications.

Results. Controlling the defect state emission via arylfunctionalized SWCNTs allows generating single photons at room-temperature within a 200 nm wide spectral range.<sup>22</sup> Therefore, to effectively improve the photon emission rate by utilizing the Purcell effect, a broad-band nanocavity is required that can cover the entire emission wavelength range. To this end, it was already shown that plasmonic nanocavities operating in the visible range can cover a bandwidth of 100-200 nm. 18-20 To extend the utility of plasmonic gapmode resonators from visible to operation at telecom wavelengths, we have designed arrays of gold nanocubes via finite-difference time-domain (FDTD) simulations that support modes in the 1100-1300 nm band (Figure 1a). At these wavelengths, the cavity mode covers the exciton emission for both  $E_{11}^*$  and more strongly red-shifted  $E_{11}^{*-}$  defect states that typically arise as the result of multiple possible aryl binding configurations.<sup>24</sup> In this way, the spectral resonance condition between emitter and cavity mode is automatically

Figure 1b shows a schematic of the assembled cavity consisting of two basic building blocks. The top block consists

of Au nanocube arrays on a transparent sapphire substrate with functionalized (6,5) SWCNTs deposited via drop casting. In this configuration, one can characterize the optical properties of the SWCNTs that are not yet coupled to the plasmonic nanocavities. After attaching the bottom block consisting of a planar Au mirror and a dielectric spacer layer of Al<sub>2</sub>O<sub>3</sub>, a plasmonic gap mode is formed with a gap size of about 5 nm, defining the coupled state of the preregistered quantum emitters. At these small distances, values for the electrical field enhancement of up to 800 are found from FDTD simulations for the in-plane nanogap mode that couples well to the exciton dipole in the SWCNT (see Supporting Information, Figure S3). The nanocube arrays are fabricated via electron beam lithography (see Methods) with a high area filling factor of 65% to optimize spatial coupling between emitter and mode (Figure 1c). The wide-field image in Figure 1d shows that exciton emission from SWCNTs residing in the plasmonic array region is drastically brighter as compared to those residing outside of the array.

We focus our study on those SWCNTs that emit as bright spots in the wide-field image, indicating that they are effectively coupled to the plasmonic gap mode. Using this map as a guide, we recorded local micro-PL spectra and quantum emission characteristics of individual SWCNTs. The corresponding signatures of single-photon antibunching recorded at 300 K appear to be extremely clean with secondorder photon correlation values at zero delay time of  $g^{(2)}(0) =$  $0.01 \pm 0.005$  (Figure 2a), corresponding to a 99% pure single photon stream even under a moderately high excitation power of 2  $\mu$ W. Such a high degree of photon antibunching is remarkable among SPE materials being capable of emitting at room temperature, which is a direct consequence of the energetically deep trapping potential in aryl-functionalized SWCNTs. Note that no spectral filtering beyond laser stray light rejection was required here because within the detection volume only one spectral peak from one quantum emitter appeared (Figure 1a). Figure 2b shows the pump power dependence of defect-state PL intensity, comparing coupled (red symbols) and uncoupled SWCNTs (blue symbols). The integrated photon count rate under continuous wave (CW) excitation and near saturation is found to be up to 52-fold enhanced for the coupled case. Although some of the coupled SWCNTs saturate at lower photon count rates, they are all at least 1 order of magnitude enhanced compared to the

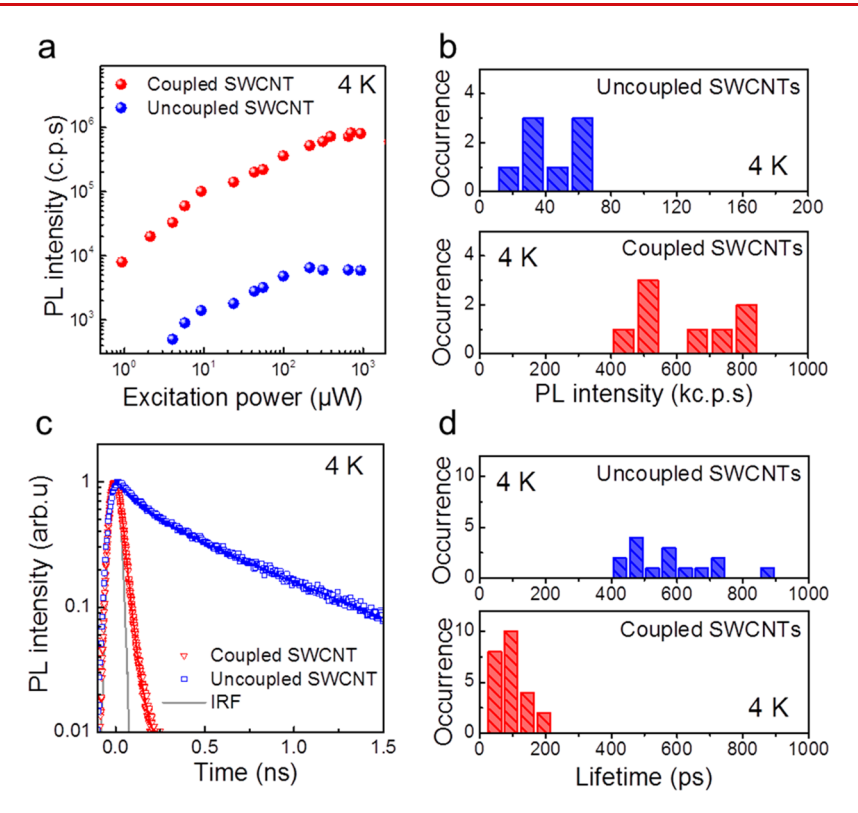


Figure 3. Low-temperature characterization of sp<sup>3</sup> defect-state emission from aryl-functionalized (6,5) SWCNTs coupled to plasmonic nanocavites. (a) Excitation power dependence of photoluminescence intensity from SWCNTs coupled (red spheres) and uncoupled (blue spheres) to plasmonic nanocavities under CW excitation. (b) Occurrence histograms of PL intensity in the saturation regime for uncoupled (upper panel) and coupled (lower panel) cases. (c) Time-resolved photoluminescence intensity of SWCNTs in the uncoupled (blue squares) and coupled state (red triangles). Blue and red solid lines are deconvolution fits that yield monoexponential decay times of  $\tau_{\text{off,LT}} = 726 \pm 12$  ps and  $\tau_{\text{on,LT}} = 10 \pm 4$  ps. IRF: Instrument response function. (d) Occurrence histograms of  $T_1$  lifetime of uncoupled (upper panel) and coupled (lower panel) cases.

uncoupled case. Driving the SPE under CW excitation, which can be considered as the ultimate limit of excitation rate, we determine a photon generation rate of 1.3 GHz into the first lens (Supporting Information, Supplementary Note 2).

To directly quantify the underlying Purcell enhancement of the coupled system we determined the total rate enhancement factor  $\gamma_{op}/\gamma_{off}$  via time-resolved photoluminescence (TRPL) measurements, where  $\gamma_{\rm on}$  and  $\gamma_{\rm off}$  are the emission rates for the coupled and uncoupled case, respectively. Figure 2c shows the time-correlated single photon counting (TCSPC) traces for exemplary SWCNTs with monoexponential decay times of  $au_{\rm off,RT}$  = 588  $\pm$  10 ps and  $au_{\rm on,RT}$  = 11  $\pm$  3 ps, yielding a rate enhancement of  $\gamma_{\text{on,RT}}/\gamma_{\text{off,RT}} = 53$ . Taking into account the known quantum yield (QY) for uncoupled defect state emission of 13%, 22 one can determine a Purcell factor of  $F_p = 300$  for this emitter (see Supporting Information, Supplementary Note 3). These strong Purcell factors are a hallmark of plasmonic nanocavities and are significantly larger as compared to aryl-functionalized SWCNTs coupled to dielectric cavities with reported rate enhancements limited to about 30%.32 As a result, under cavity-coupling and roomtemperature conditions, we determine an unprecedented SE rate of 11 ps for a solid-state SPE.

The strong Purcell effect and significantly reduced  $T_1$  time observed here advances SWCNT SPEs toward the critical goal of indistinguishable single photon emission. To also lengthen the  $T_2$  dephasing time with the goal of reaching the Fourier transform limit of emitted photons, one can effectively avoid exciton—phonon dephasing by cooling the sample to cryogenic temperatures. Figure 3 shows that pronounced Purcell

enhancement is still present at 4 K, as characterized by an intensity enhancement up to 133 (Figure 3a), with an ensemble average of 14.5 (Figure 3b). Time-resolved measurements reveal  $\tau_{\rm off,LT}$  = 726  $\pm$  12 ps and  $\tau_{\rm on,LT}$  = 10  $\pm$  4 ps, implying a rate enhancement up to  $\gamma_{\text{on,LT}}/\gamma_{\text{off,LT}}$  = 73 that corresponds to  $F_p$  = 415 and a cavity-enhanced QY of 74% in the best case (Figure 3c). Note that the cavity-coupling scheme is spectrally and spatially autocoupling because every deposited SWCNT shows significant Purcell enhancement, as is evident from the ensemble average of 24 SWCNTs that display uncoupled lifetime values of 575 ps that reduce to 96 ps under coupling (Figure 3d). At  $T_1$  values of 10 ps for the coupled case, the radiative recombination of the exciton contributes 66  $\mu$ eV to the emitter line width calculated via the uncertainty principle, as shown by the blue dashed line in Figure 4a. Using the full width at half-maximum (fwhm) of the measured spectral line width value of 105  $\pm$  5  $\mu$ eV (Figure 4a), and the well-known relation fwhm  $=\frac{2\hbar}{T_2}=\frac{\hbar}{T_1}+\frac{2\hbar}{T_2^*}$ , where  $T_2$ is the overall dephasing time and  $T_2^*$  is pure dephasing time, one can extract a contribution of  $T_2^*$ = 34.1 ps to the line width broadening, as well as  $T_2 = 12.6$  ps. As a result, one can estimate a TPI visibility  $T_2/2T_1$  = 0.63, indicating that the emitted single photons are nearly Fourier transform limited, if the sample is held at 4 K. In contrast, when operated at room temperature the strong exciton dephasing ( $\sim$ 50 fs) reduces the expected TPI visibility to only 0.002, that is, a regime that would require a much stronger Purcell effect to become observable (Supporting Information, Supplementary Note 4).

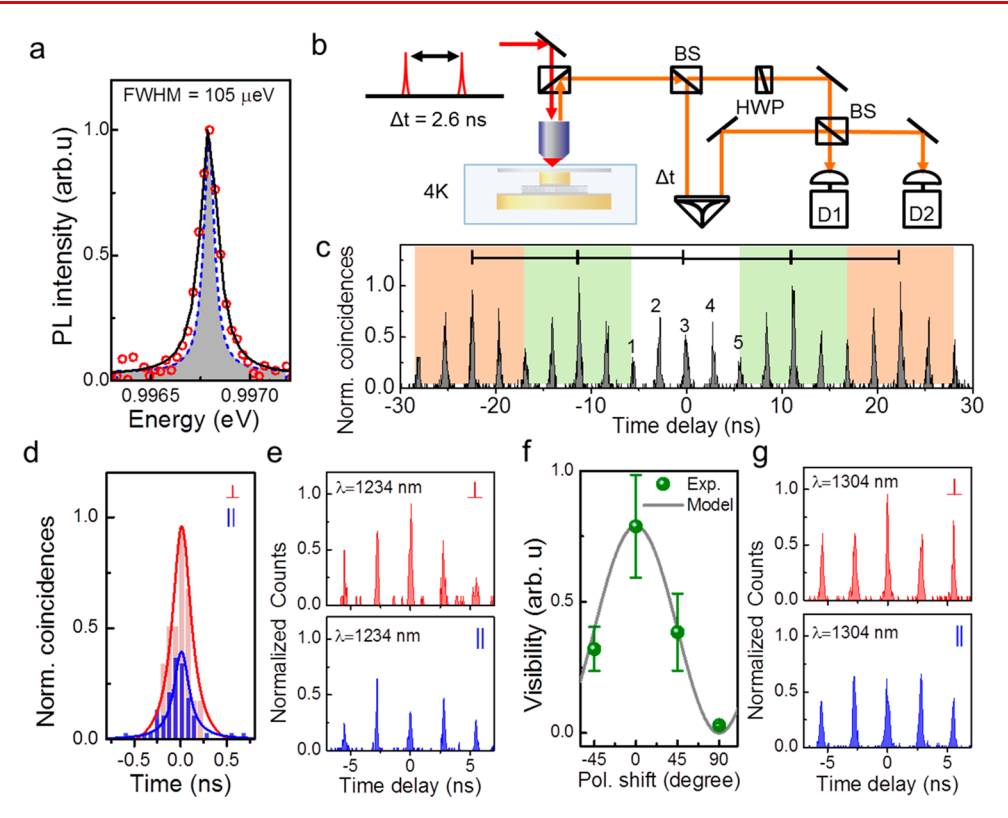


Figure 4. Demonstration of single-photon indistinguishability. (a) Photoluminescence spectrum of  $E_{11}^{*-}$  emission recorded at 4 K under an excitation power of 10  $\mu$ W. Experimental data (red circles) are fitted with a Lorentzian (black solid line) with a fwhm of  $105 \pm 5 \mu$ eV. Blue dash line: calculated contribution of  $T_1$  homogeneous (lifetime) broadening. (b) Schematic of Hong-Ou-Mandel interferometer setup with 2.6 ns double-pulse excitation. BS: Beam splitter, HWP: Half wave plate. (c) Coincidence histogram recorded with a bin size of 1 ps. Colored regions indicate laser repetition rate that repeats the five-peak pattern centered at -22, -11, 0, 11, and 22 ns. (d) Direct comparison of the quantum interference at zero delay time under crossed-polarization (red) and parallel-polarization (blue). (e) Two-photon interference recorded with cross-polarization (upper panel) and parallel-polarization shift between the photons in the two arms. (g) TPI histogram recorded with cross-polarization (upper panel) and parallel-polarization (lower panel) for telecom O-band emission at 1304 nm.

The expected TPI value determined in this way can a priori underestimate the achievable degree of single-photon indistinguishability because the dephasing time extracted from the time-integrated spectral line width measurement averages over many rapid spectral diffusion processes. In contrast, direct measurements in the time-domain with a Hong-Ou-Mandel (HOM) type of interferometer can overcome this limitation because consecutively emitted photons from the SPE are brought in temporal overlap on fast time scales of a few nanoseconds.<sup>33</sup> In our setup, a 2.6 ns delayed double pulsed excitation creates two photons from the SWCNT that are routed through a HOM interferometer (Figure 4b). The resulting correlation histogram shown in Figure 4c depicts five possible temporal channels labeled 1-5 with channels 1 and 5 representing early-early and late-late events, channels 2 and 4 represent late-early and early-late events, whereas channel 3 measures TPI events in temporal overlap.<sup>34</sup> This five-peak pattern is repeated every 11.2 ns (89 MHz laser repetition rate) as indicated by the shading. To demonstrate that the single photons have nearly identical wave packets, one can compare the coincidence intensities for simultaneous arrival peaks (peak 3) for the cases where the two photons have either (1) the same polarization state and undergo interference or (2) orthogonal polarization where they cannot interfere. Figure 4d shows a significantly reduced peak area for the case where the two consecutively triggered photons have identical polarization states. To directly determine the TPI visibility without relying

on post selection, one can compare the intensity of the zero delay time peak 3 with peaks 2 and 4 which creates a conditional probability that detects only the events where photons leave the beam splitter in opposite directions, that is, do not undergo photon bunching, as is the case for indistinguishable photons. In this case the TPI visibility can be determined from  $^{34,35}$ 

$$V = \frac{1}{(1 - \varepsilon)^2} \left[ 2g^{(2)}(0) + \frac{R^2 + T^2}{2RT} - \frac{A_3}{A_2 + A_4} \left( 2 + g^{(2)}(0) \frac{R^2 + T^2}{RT} \right) \right]$$

where  $A_2$ ,  $A_3$ , and  $A_4$  are the areas of peak 2, 3, and 4, respectively, R=0.55 the reflectivity and T=0.45 the transmissivity of the beam splitter, and  $1-\varepsilon$  is the maximum fringe visibility of the interferometer as determined from laser light (Figure 4e). As a result, a pronounced TPI visibility of  $V=0.79\pm0.20$  can be estimated for the exciton emission at 1240 nm and low optical pump power of 150 nW (see Supporting Information, Supplementary Note 5). As a key result, the TPI visibility of an initially largely incoherent SPE characterized by V=0.008 has been increased in our coupling scheme by a factor of 99, that is, by almost 2 orders of magnitude.

The TPI visibility follows the expected  $\cos(\theta)^2$  dependence when rotating the polarization of the photons at the input port of the beam splitter from parallel to orthogonal orientation (Figure 4f). Moreover, we also observed indistinguishable

single photon emission from SWCNT defect states at the longer wavelength of 1304 nm that is directly in the telecom O-band, albeit with a slightly reduced visibility of  $V = 0.40 \pm$ 0.06 (Figure 4g). Likewise, at the shorter emission wavelength of 1154 nm we prove TPI from single photons with a visibility of  $V = 0.60 \pm 0.04$  (see Supporting Information, Supplementary Figure 5). Note that in these two cases the emitter wavelength resides away from the center of the plasmonic resonance (Figure 1a), thereby creating a reduced Purcell effect that is responsible for the reduced visibility. It is nevertheless remarkable that our plasmonic gap-mode resonators sustain single photon indistinguishability over an extremely broad bandwidth of  $\Delta \lambda = 150$  nm. The highest observed TPI visibility of 79% significantly outperforms previous attempts to utilize SPE, such as InP QDs, 16 to generate indistinguishable photons directly at telecom bands and without relying on lossy quantum frequency conversion (Supporting Information, Supplementary Note 1). In this way, our results demonstrate that plasmonic gap-mode nanocavities can overcome quantum decoherence, particularly for quantum emitters that suffer initially from strong dephasing, as was recently predicted.17

In summary, by coupling aryl-functionalized (6,5) SWCNTs to plasmonic nanocavities we demonstrate an on-chip telecomband quantum light source that operates at room temperature with unprecedented quantum yield up to 74% and purity up to 99%, and when cooled to 4 K it enables transformation of initially incoherent single photons into a coherent output stream characterized by a high TPI visibility up to 0.79. Importantly, high photon indistinguishability has been achieved without post selection and within the telecom wavelength range over a 150 nm bandwidth that can enable frequency multiplexing in future quantum networks, here for a 1D nanostructure featuring excellent optical tunability at the molecular level. If required, the TPI visibility can be further optimized through resonant excitation that increases the coherence time and reduces the timing jitter and charge noise<sup>35,36</sup> and thus ultimately enables advanced quantum information processing. Furthermore, our demonstration of a coherent quantum light source directly in the telecom O-band is particularly important, given that recent advances in practical implementation of QKD separates the classical channel required for authentication and bit error rate determination to the C-band, whereas the quantum channel resides in the Oband to avoid crosstalk.<sup>37</sup> As such, high TPI visibility within the O-band is directly relevant for the technological platforms envisioned for quantum logic applications.

**Method.** Plasmonic Nanocavity Fabrication. The Au nanocube arrays were fabricated by an Elionix ELS-G100 electron-beam lithography (EBL) system using 495 poly(methyl methacrylate) A4 (MicroChem) and developed in MIBK/IPA at a ratio of 1:3 for 180 s. To form the nanocubes, a 5 nm Ti adhesion layer and a 30 nm Au layer were deposited on the samples with an electron beam evaporator (AJA Orion 3-TH). The remaining resist is then stripped with warm acetone at 50 °C for 10 min. To create the plasmonic spacer, we used atomic layer deposition to form a 2 nm Al<sub>2</sub>O<sub>3</sub> layer on top of the samples. To form the planar Au mirror, a 5 nm Ti adhesion layer and a 100 nm Au layer were deposited by slowrate electron beam evaporation onto an epi-ready sapphire substrate.

Numerical Simulation. Finite-difference time-domain (FDTD) simulations were carried out using Lumerical

FDTD Solutions software package to determine the physical dimensions that result in plasmon resonance energies that match with the known emission energy of the exciton emission from the defect states. A total-field scatter-field source was used to excite the plasmonic structures and a simulation region with 1 nm uniform mesh size in x-, y-, and z-directions was defined. Frequency-domain field and power monitors were placed near the sample surface to record the near-field electrical field intensity shown in Supporting Information, Figure S3.

SWCNT Sample Preparation. PFO-bpy (poly[(9,9-dioctylfluorenyl-2,7-diyl)-alt-co-(6,6')-{2,2'-bipyridine})]) wrapped (6,5) SWCNTs were synthesized by the laser vaporization process and isolated in toluene suspensions by a separation method as described previously.<sup>26</sup> The functionalization method is based on a dip-doping process. Diluted SWCNT samples in toluene were first drop-casted on the nanoplasmonic substrate and dried out in air for a few minutes. The substrate was then immersed into aqueous solution of 3,5diclorobenzene diazonium (doping concentration ~1.5 mg/ mL in DI water) for 10 min. The reaction was stopped by switching the substrate into pure DI water for 1 min followed by flushing with isopropyl alcohol for another 1 min. Next, the substrate was immersed into hexadecane (from Sigma-Aldrich with product number #296317) for 10 min. Finally, the substrate was rinsed by toluene for 30 seconds to remove excess PFO polymer.

Optical Measurements. All spectroscopy experiments were performed with a home-built micro-PL system either at room temperature or at a cryogenic temperature of 4-5 K. A Ti:sapphire laser operating at 845 nm in continuous wave mode was used to excite (6,5) SWCNTs via an  $E_{11}$  phonon sideband. A 50× infrared objective (Olympus) with numerical aperture NA = 0.65 was used to focus the laser beam and collect the PL signal. PL signals were recorded with a twodimensional InGaAs array camera for imaging and a onedimensional InGaAs linear array detector for spectra analysis, respectively. For Hanbury-Brown-Twiss experiments, the Ti:sapphire laser operating under pulsed condition with a repetition rate of 89 MHz and a wavelength of 845 nm was used to excite the SWCNTs. The PL signal was then coupled into an optical fiber and sent to a 50:50 optical fiber beamsplitter to split the signal into two channels of a superconducting nanowire single-photon detector (Single Quantum Eos 210). PL time traces, decay curves, and  $g^{(2)}(\tau)$ functions were obtained with the HydraHarp time-correlated photon-counting electronics. For two-photon interference measurements, a Hong-Ou-Mandel interferometer setup was used with a laser pulse separation of 11.2 ns (i.e., 89 MHz repetition rate) that was doubled with a fixed 2.6 ns long fiber delay to create twin laser pulses for double-excitation of the quantum emitter. In the interferometer, a retroreflector mounted on a motorized stage acts as a variable mechanical delay for one optical path in order to compensate the 2.6 ns long pulse delay and establish temporal overlap of the photons with highest TPI visibility. The time delay on the x-axis in Figure 4c is the relative arrival time delay between start and stop photons, that is, the TPI trace is recorded without moving the retro mirror.

### ASSOCIATED CONTENT

## S Supporting Information

The Supporting Information is available free of charge on the ACS Publications website at DOI: 10.1021/acs.nanolett.9b04069.

(PDF)

# AUTHOR INFORMATION

# **Corresponding Authors**

\*E-mail: htoon@lanl.gov. \*E-mail: strauf@stevens.edu.

#### ORCID ®

Yue Luo: 0000-0002-2757-5395 Xiaowei He: 0000-0002-4982-8250

Jeffrey L. Blackburn: 0000-0002-9237-5891 Stephen K. Doorn: 0000-0002-9535-2062 Han Htoon: 0000-0003-3696-2896 Stefan Strauf: 0000-0002-9887-7059

# **Author Contributions**

S.S. and Y.L. designed the experiment. Y.L fabricated the plasmonic chips. J.L.B. synthesized the SWCNTs. X.H. performed the SWCNT aryl-functionalization and dispersion. Y.L., X.H., and Y.K. performed the optical experiments and analyzed the data. S.S., S.D., and H.H. supervised the functionalization and optical experiments. S.S. and Y.L. cowrote the paper. All authors discussed results and commented on the manuscript.

#### Notes

The authors declare no competing financial interest.

# ■ ACKNOWLEDGMENTS

This work was performed in part at the Advanced Science Research Center Nano Fabrication Facility of the Graduate Center at the City University of New York and also in part at the Center for Integrated Nanotechnologies, a U.S. Department of Energy Office of Science user facility. The authors acknowledge financial support to S.S. from the National Science Foundation (NSF) under awards DMR-1506711 and DMR-1809235. S.S. acknowledges financial support for the attoDRY1100 under NSF award ECCS-MRI-1531237. X.H., Y.K., and S.K.D. acknowledge partial support from the LANL LDRD program. H.H. acknowledges partial support from DOE BES FWP#LANLBES22. This work was authored in part by the National Renewable Energy Laboratory, operated by Alliance for Sustainable Energy, LLC, for the U.S. Department of Energy (DOE) under Contract No. DE-AC36-08GO28308. Funding for J.L.B. provided by the Solar Photochemistry Program, Division of Chemical Sciences, Geosciences, and Biosciences, Office of Basic Energy Sciences, U.S. Department of Energy (DOE).

# **■** REFERENCES

- (1) Aharonovich, I.; Englund, D.; Toth, M. Nat. Photonics 2016, 10, 631–641.
- (2) Senellart, P.; Solomon, G.; White, A. Nat. Nanotechnol. 2017, 12, 1026–1039.
- (3) He, X.; Htoon, H.; Doorn, S. K.; Pernice, W. H. P.; Pyatkov, F.; Krupke, R.; Jeantet, A.; Chassagneux, Y.; Voisin, C. *Nat. Mater.* **2018**, *17*, *663*–*670*.
- (4) Pant, M.; Krovi, H.; Englund, D.; Guha, S. Phys. Rev. A: At., Mol., Opt. Phys. 2017, 95, 012304.

- (5) Maurer, P. C.; Kucsko, G.; Latta, C.; Jiang, L.; Yao, N. Y.; Bennett, S. D.; Pastawski, F.; Hunger, D.; Chisholm, N.; Markham, M.; Twitchen, D. J.; Cirac, J. I.; Lukin, M. D. Science 2012, 336, 1283–1286.
- (6) Azuma, K.; Tamaki, K.; Lo, H.-K. Nat. Commun. 2015, 6, 7787.
- (7) Gazzano, O.; Vasconcellos, S. M. de; Arnold, C.; Nowak, A.; Galopin, E.; Sagnes, I.; Lanco, L.; Lematre, A.; Senellart, P. *Nat. Commun.* **2013**, *4*, 2434.
- (8) Laurent, S.; Varoutsis, S.; Gratiet, L. L.; Lematre, A.; Sagnes, I.; Raineri, F.; Levenson, A.; Robert-Philip, I.; Abram, I. *Appl. Phys. Lett.* **2005**, *87*, 163107.
- (9) Liu, F.; Brash, A. J.; O'Hara, J.; Martins, L. M. P. P.; Phillips, C. L.; Coles, R. J.; Royall, B.; Clarke, E.; Bentham, C.; Prtljaga, N.; Itskevich, I. E.; Wilson, L. R.; Skolnick, M. S.; Fox, A. M. Nat. Nanotechnol. 2018, 13, 835–840.
- (10) Weber, J. H.; Kambs, B.; Kettler, J.; Kern, S.; Maisch, J.; Vural, H.; Jetter, M.; Portalupi, S. L.; Becher, C.; Michler, P. *Nat. Nanotechnol.* **2019**, *14*, 23–26.
- (11) Aharonovich, I.; Castelletto, S.; Simpson, D. A.; Su, C.-H.; Greentree, A. D.; Prawer, S. Rep. Prog. Phys. 2011, 74, 076501.
- (12) Castelletto, S.; Johnson, B. C.; Ivády, V.; Stavrias, N.; Umeda, T.; Gali, A.; Ohshima, T. Nat. Mater. 2014, 13, 151-156.
- (13) Tran, T. T.; Bray, K.; Ford, M. J.; Toth, M.; Aharonovich, I. *Nat. Nanotechnol.* **2016**, *11*, 37–41.
- (14) Zhou, Y.; Wang, Z.; Rasmita, A.; Kim, S.; Berhane, A.; Bodrog, Z.; Adamo, G.; Gali, A.; Aharonovich, I.; Gao, W. Sci. Adv. 2018, 4, No. eaar3580.
- (15) Wang, J.; Zhou, Y.; Wang, Z.; Rasmita, A.; Yang, J.; Li, X.; von Bardeleben, H. J.; Gao, W. Nat. Commun. 2018, 9, 4106.
- (16) Kim, J.-H.; Cai, T.; Richardson, C. J. K.; Leavitt, R. P.; Waks, E. Optica 2016, 3, 577.
- (17) Bogdanov, S. I.; Boltasseva, A.; Shalaev, V. M. Science 2019, 364, 532-533.
- (18) Akselrod, G. M.; Argyropoulos, C.; Hoang, T. B.; Cirac, C.; Fang, C.; Huang, J.; Smith, D. R.; Mikkelsen, M. H. *Nat. Photonics* **2014**, *8*, 835–840.
- (19) Luo, Y.; Shepard, G. D.; Ardelean, J. V.; Rhodes, D. A.; Kim, B.; Barmak, K.; Hone, J. C.; Strauf, S. *Nat. Nanotechnol.* **2018**, *13*, 1137–1142.
- (20) Luo, Y.; Ahmadi, E. D.; Shayan, K.; Ma, Y.; Mistry, K. S.; Zhang, C.; Hone, J.; Blackburn, J. L.; Strauf, S. *Nat. Commun.* **2017**, 8, 1413
- (21) Ma, X.; Hartmann, N. F.; Baldwin, J. K. S.; Doorn, S. K.; Htoon, H. Nat. Nanotechnol. 2015, 10, 671-675.
- (22) He, X.; Hartmann, N. F.; Ma, X.; Kim, Y.; Ihly, R.; Blackburn, J. L.; Gao, W.; Kono, J.; Yomogida, Y.; Hirano, A.; Tanaka, T.; Kataura, H.; Htoon, H.; Doorn, S. K. *Nat. Photonics* **2017**, *11*, 577–582.
- (23) Piao, Y.; Meany, B.; Powell, L. R.; Valley, N.; Kwon, H.; Schatz, G. C.; Wang, Y. Nat. Chem. 2013, 5, 840–845.
- (24) He, X.; Gifford, B. J.; Hartmann, N. F.; Ihly, R.; Ma, X.; Kilina, S. V.; Luo, Y.; Shayan, K.; Strauf, S.; Blackburn, J. L.; Tretiak, S.; Doorn, S. K.; Htoon, H. ACS Nano 2017, 11, 10785–10796.
- (25) Khasminskaya, S.; Pyatkov, F.; Slowik, K.; Ferrari, S.; Kahl, O.; Kovalyuk, V.; Rath, P.; Vetter, A.; Hennrich, F.; Kappes, M. M.; Goltextquotesingletsman, G.; Korneev, A.; Rockstuhl, C.; Krupke, R.; Pernice, W. H. P. *Nat. Photonics* **2016**, *10*, 727–732.
- (26) Shayan, K.; He, X.; Luo, Y.; Rabut, C.; Li, X.; Hartmann, N. F.; Blackburn, J. L.; Doorn, S. K.; Htoon, H.; Strauf, S. *Nanoscale* **2018**, *10*, 12631–12638.
- (27) Hofmann, M. S.; Glückert, J. T.; Noé, J.; Bourjau, C.; Dehmel, R.; Högele, A. Nat. Nanotechnol. 2013, 8, 502-505.
- (28) Matsuda, K.; Inoue, T.; Murakami, Y.; Maruyama, S.; Kanemitsu, Y. Phys. Rev. B: Condens. Matter Mater. Phys. 2008, 77, 033406.
- (29) Sarpkaya, I.; Zhang, Z.; Walden-Newman, W.; Wang, X.; Hone, J.; Wong, C. W.; Strauf, S. *Nat. Commun.* **2013**, *4*, 2152.
- (30) He, X.; Sun, L.; Gifford, B. J.; Tretiak, S.; Piryatinski, A.; Li, X.; Htoon, H.; Doorn, S. K. *Nanoscale* **2019**, *11*, 9125–9132.

(31) Hartmann, N. F.; Velizhanin, K. A.; Haroz, E. H.; Kim, M.; Ma, X.; Wang, Y.; Htoon, H.; Doorn, S. K. ACS Nano 2016, 10, 8355–8365.

- (32) Ishii, A.; He, X.; Hartmann, N. F.; Machiya, H.; Htoon, H.; Doorn, S. K.; Kato, Y. K. *Nano Lett.* **2018**, *18*, 3873–3878.
- (33) Thoma, A.; Schnauber, P.; Gschrey, M.; Seifried, M.; Wolters, J.; Schulze, J.-H.; Strittmatter, A.; Rodt, S.; Carmele, A.; Knorr, A.; Heindel, T.; Reitzenstein, S. *Phys. Rev. Lett.* **2016**, *116*, 033601.
- (34) Santori, C.; Fattal, D.; Vuckovic, J.; Solomon, G. S.; Yamamoto, Y. *Nature* **2002**, *419*, 594–597.
- (35) Somaschi, N.; Giesz, V.; Santis, L. D.; Loredo, J. C.; Almeida, M. P.; Hornecker, G.; Portalupi, S. L.; Grange, T.; Antón, C.; Demory, J.; Gómez, C.; Sagnes, I.; Lanzillotti-Kimura, N. D.; Lematre, A.; Auffeves, A.; White, A. G.; Lanco, L.; Senellart, P. *Nat. Photonics* **2016**, *10*, 340–345.
- (36) Ates, S.; Ulrich, S. M.; Reitzenstein, S.; Löffler, A.; Forchel, A.; Michler, P. *Phys. Rev. Lett.* **2009**, *103*, 167402.
- (37) Schrenk, B.; Hentschel, M.; Hübel, H. In Optical Fiber Communication Conference (OFC) 2019; OSA, 2019.